PAPER • **OPEN ACCESS**

Interface Engineering for Enhanced Magnetic Vortex Pinning by 1D-BZO APCs in a Wide Angular Range

To cite this article: Victor Ogunjimi *et al* 2022 *IOP Conf. Ser.: Mater. Sci. Eng.* **1241** 012022

Interface Engineering for Enhanced Magnetic Vortex Pinning by 1D-BZO APCs in a Wide Angular Range

Victor Ogunjimi[1*], Mary Ann Sebastian[2,3], Di Zhang[3], Bibek Gautam[1], Jie Jian[4], Jijie Huang[4], Yifan Zhang[4], Timothy Haugan[2], Haiyan Wang[4], and Judy Wu[1]

[1]*Department of Physics and Astronomy, the University of Kansas, Lawrence, Kansas 66045, USA*
[2]*U.S Air Force Research Laboratory, Aerospace Systems Directorate, WPAFB, OH 45433, USA*
[3]*University of Dayton Research Institute, Dayton, OH 45469, USA*
[4]*School of Materials Engineering, Purdue University, West Lafayette, IN 47907, USA*

*Corresponding author E-mails: victorogunjimi@gmail.com, jwu@ku.edu

Abstract: Microstructural analysis of the $BaZrO_3$ (BZO)/$YBa_2Cu_3O_7$ (YBCO) interface has revealed a highly defective and oxygen deficient 2-3 nm thick YBCO column surrounding the BZO one-dimensional artificial pinning centers (1D-APCs). The resulting semi-coherent interface is the consequence of the ~7.7% BZO/YBCO lattice mismatch and is responsible for the low pinning efficiency of BZO 1D-APCs. Herein, we report an interface engineering approach of dynamic Ca/Cu replacement on YBCO lattice to reduce/eliminate the BZO/YBCO lattice mismatch for improved pinning at a wide angular range of the magnetic field orientation. The Ca/Cu replacement induces a local elongation of the YBCO c-lattice near the BZO/YBCO interface, thereby ensuring a reduction in the BZO/YBCO lattice mismatch to ~1.4% and a coherent BZO/YBCO interface. This has resulted in enhanced pinning at B//c-axis and a broad angular range of B-field orientation. For example, the 6 vol.% BZO/YBCO film with interface engineering exhibits F_p ~158 GN/m^3 at 65 K and B//c-axis, which is 440% higher than the ~36.1 GN/m^3 for the reference 6% BZO/YBCO sample, and enhanced J_c and F_p in a wide angular range up to ~ 80^o. This result illustrates a facile scheme for engineering 1D-APC/YBCO interface to resume the pristine pinning efficiency of the 1D-APCs.
Keywords: BZO/YBCO interface, pinning efficiency, strain field, lattice mismatch, vortex pinning

1. Introduction

Artificial pinning centers (APCs) self-assembled in $YBa_2Cu_3O_{7-x}$ (YBCO) demobilize magnetic vortices to enhance critical current density needed for high temperature superconductor (HTS) applications. One-dimensional (1D) c-axis aligned APCs like $BaZrO_3$ (BZO)[1-5], $BaHfO_3$ (BHO)[6-10], $BaSnO_3$[11, 12] $YBa_2(Nb/Ta)O_6$[13, 14] etc. have been reported to effectively pin vortices for magnetic field oriented along the c-axis. The APC material lattice mismatch with YBCO affects the pinning efficiency of the APCs. BZO 1D-APC/YBCO interface has been reported to be semi-coherent with high defect density a consequence of the ~ 7.7% BZO/YBCO lattice mismatch [15-17]. Meanwhile, a high-resolution electron microscopy study of the BZO/YBCO interface, has reported a cylindrical YBCO shell with a thickness of a few nm surrounding the BZO 1D-APCs. This region has been shown to contain a large concentration of defects such as dislocations with much reduced superconductivity due to oxygen deficiency [18]. Since the pinning force per unit length of the BZO 1D-APCs is proportional to the radial derivative of the pinning energy at the BZO/YBCO interface [19], the reduced superconductivity in this YBCO shell at the BZO/YBCO interface is expected to degrade the pinning efficiency of the BZO 1D-APCs [18]. Experimentally, considerably higher pinning efficiency, illustrated in the higher critical current density (J_c) and pinning force density (F_p),

have been observed on BHO 1D-APCs that form a coherent and almost defect-free interface with YBCO [16]. Specifically, this is illustrated in a peak of $J_c(\theta)$ centered at θ=0, or B//c-axis (θ represents the tilt angle of the B field away from the c-axis in the plane perpendicular to J_c) in the 1D-APCs/REBCO nanocomposites. A more recent study in probing the effect of the enhanced pinning efficiency of 1D-APCs on the angular range of the enhanced pinning with the pinning efficiency, through a comparison of the angular dependence of the peak pinning force density (F_{pmax}) and its location (B_{max}) on the BZO 1D APC/YBCO and BHO 1D-APC/YBCO nanocomposite films [20, 21], has revealed a broader angular range of enhanced pinning of θ>67° in the latter, suggesting the further benefit of a coherent 1D-APC/YBCO interface in reducing the J_c anisotropy with respect the B field orientations.

In order to achieve a coherent BZO/YBCO interface, this work explores reduction of the BZO/YBCO lattice mismatch via enlarging the c-axis constant of YBCO locally near the BZO 1D-APCs. Specifically, we explore a partial replacement of smaller Cu+2 ions on the Cu-O planes of YBCO lattice with larger Ca+2 ions (by 30%) for enlarged c-axis lattice constant locally through formation of planer defects or stacking faults. In order to control the amount of Ca in YBCO in the BZO 1D APC/YBCO nanocomposite films, two $Ca_{0.3}Y_{0.7}Ba_2Cu_3O_{7-x}$ (CaY-123) spacers of only 10 nm in thickness were inserted into the 2 vol.% (and 6 vol.%) BZO 1D APC/YBCO nanocomposite thin films of ~ 150 nm in thickness. In these multilayer (ML) samples consisting of three 50 nm thick BZO 1D-APC/YBCO and two CaY-123 layer each of 10 nm in thickness stacking alternatively, diffusion of Ca from the spacers into YBCO increases the c-axis lattice of the YBCO dramatically to allow coherent BZO 1D APC/YBCO interface[22] to form. This coherent interface has a profound effect on the pinning efficiency of the BZO 1D-APCs as illustrated in the almost double to quadruple of the F_p values in the ML samples as compared to the reference single-layered BZO 1D-APC/YBCO samples of the same BZO doping. In addition, significantly reduced pinning anisotropy was observed especially at high magnetic fields.

2. Experimental

Pulsed laser deposition (PLD) was used to deposit 2-6 vol.% BZO doped YBCO nanocomposite films on (100) $SrTiO_3$ (STO) single crystal substrates[1, 23, 24]. To isolate the Ca doping effect, one set consisting of single-layer (SL) YBCO films doped with 2% - 6% BZO in the range of 2-6 vol.% (2-6% BZO/YBCO-SL) were fabricated as reference samples. The other set consists of two additional Ca-containing spacer layers inserted in each BZO doped YBCO nanocomposite film to form a multi-layer (ML) structure. The ML structure has three 50 nm thick BZO doped YBCO layers separated by two ~ 10 nm thick $Ca_{0.3}Y_{0.7}Ba_2Cu_3O_{7-x}$ (CaY-123) spacers (Figure 1). The CaY-123 spacers were deposited with a PLD repetition rate of 2 Hz. All samples were deposited in 300 mTorr oxygen (O_2) at a substrate temperature of ~825 °C[1]. The BZO/YBCO layers were deposited at a repetition rate of 8 Hz in both sets of the samples. For the ease of discussion, the SL and ML samples are aliased as xSL and xML respectively where x is either 2% or 6%. Post deposition, the samples were annealed for about 30 minutes dwell time at 500 °C in one atmosphere O_2 pressure. The film thicknesses were measured using a Tencor P-16 profilometer. For electrical transport measurement, Ag contact pads were sputtered on the samples through a shadow mask. The samples were then patterned using standard photolithography (Leica) to create two microbridges of length ~500 μm and width of 20 and 40 μm respectively. The details of the patterning and sample wiring for the transport measurement can be found in our previous works.[25, 26] The samples were mounted on a oxygen-free Cu stage using Ag paste and resistance–temperature (R-T) and current-voltage (I-V) characteristic curves were measured as function of temperature T (65K-77 K) and the magnetic field B (up to 9.0 T) applied in the c-axis of the BZO/YBCO films in a Quantum Design Ever-Cool II Physical Property Measurement System (PPMS). To minimize the heating at high currents, a pulsed current source (Keithley 2430 1KW Pulse Source Meter) was adopted with the pulse width of ~ 500 ms for the I-V curves. J_c was determined by applying 1 μV/cm standard criterion.[26-28] The microstructural images of the films were acquired via Cs-corrected transmission electron microscopy (TEM) and scanning transmission electron microscopy (STEM). The TEM and STEM results were achieved using a 1.6 Å resolution Thermo Fisher Scientific TALOS F200X TEM. All STEM images were captured using a high angle annular

dark field mode (HAADF). Furthermore, a new generation Thermo Fisher Scientific microscope was used to acquire high-resolution STEM (HRSTEM) images with a resolution ~ 63 pm.

3. Results and Discussions

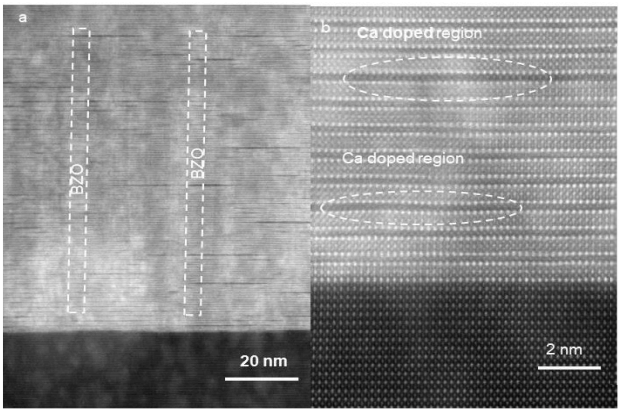

Figure 1. HRSTEM cross-section images of the ML film. Figure 1a indicate the growth of c-axis aligned BZO 1D APCs through the film's thickness. The BZO/YBCO interface lattice distortions around the APCs suggesting a coherent BZO/YBCO interface. This coherent BZO/YBCO interface occurs because of the increase in YBCO c-lattice parameter as a result of the formation of stacking faults in the Ca rich regions (enclosed in ellipse Figure 1b) due to the dynamic Ca/Cu replacement.

Figure 1 displays the HRSTEM cross-section images of the ML films. Figures 1a shows c-axis aligned BZO 1D-APCs embedded in the films. This is consistent with the expectation that Ca/Cu replacement takes place after the APCs are formed and hence would not interrupt the epitaxial growth of the APCs. Nevertheless, Figure 1a indicates that the APCs in the ML are segmented by the CaY123 spacers but the relative thinness (~ 10 nm) of the spacers may ameliorate some of the pinning detriments associated with truncated APC growth in multilayer YBCO structures with much thicker YBCO spacers [29-31]. Furthermore, significant YBCO lattice distortions are largely absent in the ML. This distortion in the YBCO lattice of SL film, which have been reported previously [32-36], arises from the strain around the BZO/YBCO interface as a result of the ~ 7.7% BZO/YBCO lattice mismatch. The absence of these defects in the ML may be attributed to the stacking faults formed in the Ca rich region (enclosed in ellipse in Figure 1b) of the ML film. The formation of the stacking faults, via Ca/Cu replacement, locally extends the YBCO c-lattice parameter thereby reducing the BZO/YBCO lattice mismatch around the BZO/YBCO interface and hence the interfacial strain.

Figure 2 compares the XRD θ-2θ spectra of 2% doped (a and b) and 6% doped(c and d) films. The black and red lines represent the SL and ML films respectively. The appearance of the YBCO (00l)

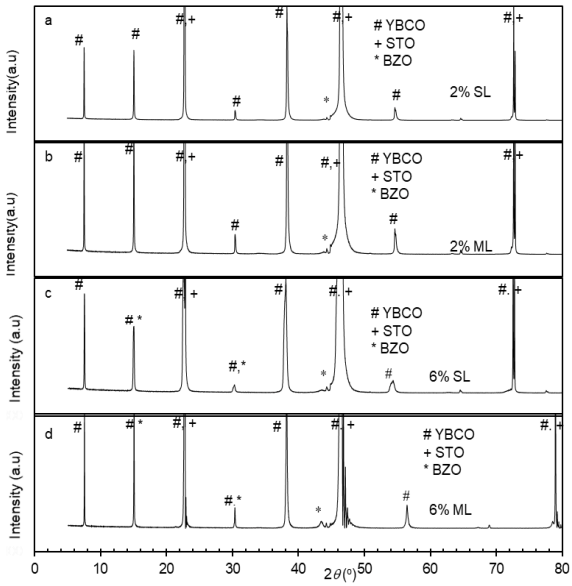

Figure 2. θ-2θ scans of SL (a and c) and ML (b and d) films at BZO doping of 2% (a and b) and 6% (c and d). The ML films were fabricated with structure or/and PLD growth conditions of: t_{spacer} =10nm, and R_{spacer} =2Hz . Cu-kα radiation of wavelength 1.54 Å was used. The symbols #, + and * represent the YBCO (001), STO substrate (100) and major BZO (001) peaks respectively.

peaks (#) confirms the c-axis orientation of the BZO/YBCO nanocomposite films on the (100) STO

substrates (+). Also, a major BZO (001) peak at ~ 46.5° appears in all three samples. The c-lattice constants were estimated from the YBCO (00l) peaks. The c-lattice constants were 11.746 Å and 11.819 Å for the 2% and 6% SL films respectively, confirming the increase in tensile strain as BZO doping concentration is increased. This increase in tensile strain is most probably due to the increased strain field overlap [37, 38]. Conversely, the same c-lattice constants of 11.766 Å observed on both the 2% and 6% ML samples may indicate a tempering down of the BZO doping induced strain field overlap effect by the ML scheme. Clearly, the enlargement of the YBCO c-axis lattice constant occurs only locally near BZO 1D-APC/YBCO and YBCO/STO interfaces due to formation of stacking faults induced by Ca/Cu replacement on Cu-O planes as revealed in the HRSTEM study in Figures 1b.

Figure 3 is the J_c (*B*) and F_p (*B*) curves of the 2% doped films (3a-3c) and 6% doped films (3d-3f) along various orientations of *B* at 65 K. The SL films (open symbols) are compared to the ML films (solid symbols) at *B*//c (Figures 3a-3b and 3d-3e) and at other *B* orientations (Figures3c and 3f). Comparisons of J_c (*B*) and F_P (*B*) curves along *B//c* confirm enhancement of pinning for magnetic field applied along the c-axis. The F_P (*B*) data taken along other *B* orientations confirm the extension of the pinning enhancement beyond *B*//c. For the 2% doped films, J_c enhancement can be observed over the entire *B* field range up to 9.0 T. For example, at 1.0 T, 5.0 T and 9.0 T, the corresponding J_c values of 4.39 MA/cm^2, 1.58 MA/cm^2 and 0.59 MA/cm^2 for the ML sample are respectively about 1.7, 1.8 and 2.7 times of that of the SL film. Qualitatively, both F_P (*B*) curves exhibit an inverted bell shape with a peak value of F_{pmax} located at B_{max} (Figure 3b). Interestingly, the 2% ML and 2% SL samples have comparable B_{max} values of 3.0 T, which is smaller than the accommodation field (~5.0 T) calculated from $B^* = n^*\Phi_o$, based on the flux quantum $\Phi_o \sim 2.07*10^{-15}$ Wb and areal density n^* of the BZO 1D-APCs acquired from TEM characterization[1, 16]. Therefore, the insertion of the CaY-123 spacer layer does not seem to affect the self-assembly of the BZO 1D-APCs in the 2% ML samples. The F_{pmax} along *B*//c of ~ 97.7 GNm^{-3} for the 2% ML sample at 65 K is 1.7 times of the F_{pmax} of ~ 57.1 GNm^{-3} in the 2% SL sample and surpasses the ~ 80 GNm^{-3} of the 2% BHO-YBCO SL sample [16]. It should be noted that the F_{pmax} values for the 2% SL sample are comparable to that reported in literature [5, 39-41]. Indeed, Ca2+/Y3+ substitution could be energetically preferred in strain-free or low-strain conditions at low BZO doping. This means that Ca/Cu and Ca/Y substitutions may occur simultaneously in the 2 vol.% BZO doped BZO/YBCO nanocomposite films with the former near the BZO 1D-APC/YBCO interface as confirmed in Fig. 1 while the latter, away from the interface. The Ca/Y substitution is well known to overdope YBCO as illustrated typically in the T_c decrease with the

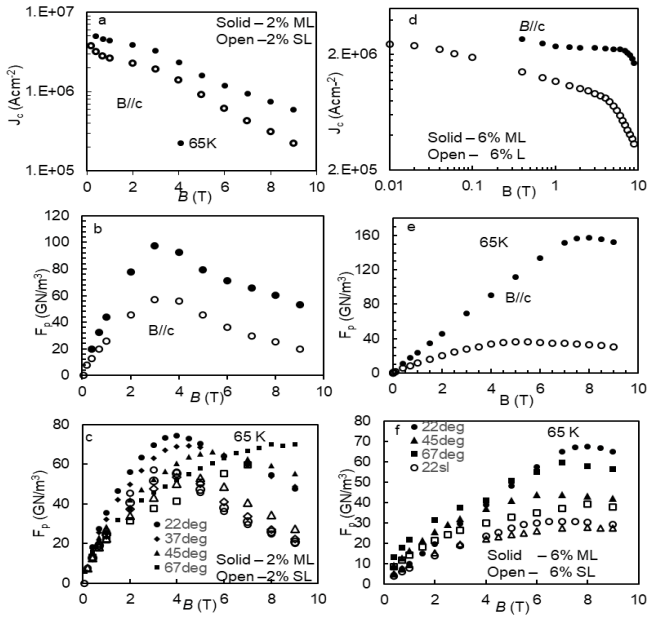

Figure 3. Transport data on the 2% doped (3a-3c) and 6% doped (3d-3f) films at 65K. The SL films (open symbols) are compared to the ML films (solid symbols) at *B*//c (3a-3b and 3d-3e) and at other *B* orientations (3c and 3f). Comparisons of J_c (*B*) and F_p (*B*) curves along *B//c* confirm enhancement of pinning for magnetic field applied along the c-axis. The F_P (*B*) data taken along other *B* orientations confirm the extension of the pinning enhancement beyond *B*//c.

substitution. Based on the moderately lower Tc of 87.5 K which is ~ 1 K lower than that of its SL

counterpart's, we suspect the Ca/Y substitution induced overdoping effect (negative) is minor. This argument is consistent with the in-field pinning enhancement in 2 % ML over the 2% SL counterpart.

Therefore, the improved pinning by the BZO 1D-APCs in the 2% BZO-YBCO ML sample could be attributed to the coherent BZO/YBCO interface of the ML film. The data indicate that the enhancement of pinning in the 2% ML film clearly extends beyond 0°. The pinning improvement in the 2% ML sample is illustrated in the overall higher F_P values almost over the entire B field range (Figures 3b-3c). The F_{pmax} along 22° - 67° in the 2% ML samples are larger than the corresponding values in the 2% BZO-YBCO SL film. For example, along 22° F_{pmax} is ~ 74.3 GNm^{-3} for the 2% BZO-YBCO ML and only 55.3 GNm^{-3} for the 2% BZO-YBCO SL sample. Also, along 67°, the F_{pmax} of ~ 70.0 GNm^{-3} measured on the 2% BZO-YBCO ML is ~70% more than the value measured on the 2% SL film. This pinning enhancement close to the ab-plane may be largely attributed to the ab-plane aligned stacking faults generated by the Ca/Cu replacement in YBCO. The extension of pinning enhancement beyond B//c is not limited to the 2% ML as can be seen in the J_c (B) and F_P (B) data on the 6% doped films in Figures 3d-3f. Similar to the 2% doping case along B//c, 6% ML sample exhibits enhanced $J_c(B)$ over the entire B field range of 0-9 T as compared to their 6% SL film and the enhancement increases with the applied B fields (Figure 3d). For example, an enhancement factor of 2.0 and 5.0 can be observed at B= 1.0 T and 9.0 T respectively (Figure 3d). Clearly, $J_c(B)$ curve for the 6% ML sample exhibits much reduced B-field susceptibility as compared with the 2% ML film and hence more enhanced pinning in a larger B field range. This is expected as the 6% ML film has three times the concentration of the BZO 1D-APCs as the 2% ML sample. The improved $J_c(B)$ leads to an improved $F_p(B)$ in the ML samples as shown in Figure 3e. While the B_{max} is similar in the 2% doped films, the enhanced B_{max} ~ 8.0 T along B//c in the 6% ML sample is 60% more than that of the 6% SL sample. Furthermore, the enhanced F_{pmax} ~ 158 GN/m^3 in the 6% ML sample (which is more than 4 times that of the 6% SL sample) is the best reported so far in BZO 1D-APC/YBCO nanocomposites films[5, 17, 42-45]. Figure 3f indicates that, similar to the 2% ML, pinning benefits in the 6% ML extends well beyond B//c and up to ~ 67°. As mentioned above, this extension of benefits close to the ab plane may be attributed to the formation of 2D planar defects induced by the Ca doping.

As a further confirmation of the extension of improved pinning beyond B//c in ML films, Figure 4a-

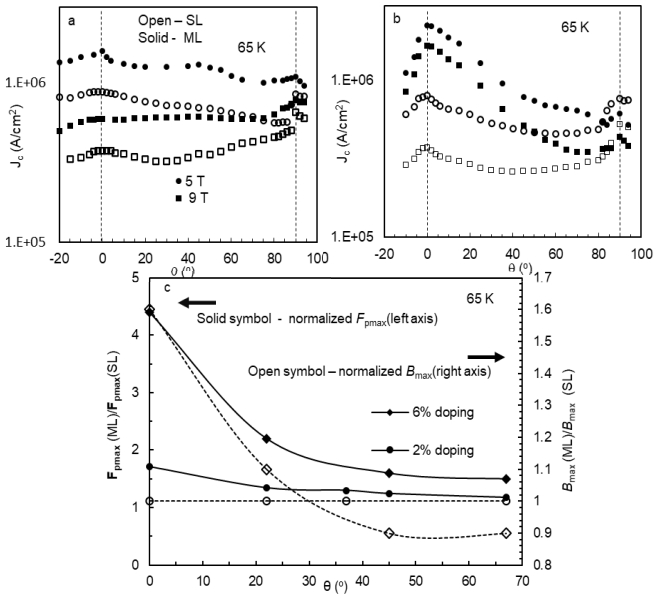

Figure 4. The pinning properties of the films at 65K. J_c (θ) data on 2% doping (a) and 6% doping (b) in 5 T (circle) and 9 T (square). Open and solid symbols represent single-layer (SL) and multilayer (ML) films respectively. (c) The normalized (the ML film data normalized to that of the SL film) $F_{P,max}$ (solid symbols and left axis) and normalized B_{max} (open symbols and right axis) as a function of (θ). Circle and diamond represent 2% doped and 6% doped film respectively.

4b compares the J_c (θ, 65K) data for the samples in Figure 3. The 2% (Figures 4a) and 6% (Figures 4b) are compared at 5.0 T (circle) and 9.0 T (square). The solid and open symbols correspond to the ML and SL films respectively. Essentially, each ML film has higher J_c than its corresponding SL sample over the entire θ range. Case in point, the maximum $J_c(\theta \leq 85°)$ of 2% ML sample is almost double and about 1.5 times that of the 2% SL film at 5.0 T and 9.0 T respectively. J_c (θ) enhancement

is even more pronounced at a higher BZO doping of 6 vol.%. In the range $\theta \leq 85^{o}$, enhancement factors as high as 2.8 and 4.5 are seen at 5.0 T and 9.0 T respectively. Furthermore, the $F_{p,max}$ values of the ML were normalized to that of the SL counterpart at different θ angles. In Figure 4c the normalized $F_{p,max}$ values (solid symbol and left axis) at 65K were plotted as function of θ for 2% (circle) and 6% (diamond). The data shows a monotonic decrease in the normalized $F_{p,max}$ with θ and the highest enhancement factors along B//c of 1.7 and 4.4 for the 2% ML and 6% ML respectively. When B is oriented to ~ 67° these factors are reduced to ~ 1.0 and 1.5 respectively. Similar to the $F_{p,max}$, the normalized B_{max} (open symbol and right axis) was calculated and plotted on the same figure (Figure 4c). In contrast to $F_{p,max}$, the B_{max} enhancement is largely insignificant (enhancement factor mostly ~ 1.0) for both BZO doping levels. The only significant B_{max} enhancement is the 1.6 value observed along B//c for the 6% ML film. The dramatic enhancement $F_{p,max}$ and B_{max} along B//c in the 6% ML sample is not surprising considering the expected benefits of improved BZO/YBCO interface and reduced strain field overlap at high concentration of the BZO 1D APCs. This angular enhancement in ML films is comparable to what has been reported on the BHO/YBCO nanocomposite films in which the 1D-APC/YBCO interface is coherent[20, 21].

4. Conclusions

In summary, a Ca doped BZO/YBCO nanocomposite ML scheme has been employed to extend angular width of pinning to ~ 67° - 85° for 2% and 6% BZO doped YBCO nanocomposites by promoting the formation of stacking faults and coherent BZO/YBCO interfaces. The Ca source is provided from the two ~10 nm thick CaY-123 spacers inserted into the 2% and 6% BZO/YBCO nanocomposite films of 150 nm in total thickness to form the ML structures. The coherent interface was induced by a reduction in the lattice mismatch at the BZO/YBCO interface as a result of the formation of the stacking faults. Microstructural analysis using HRSTEM confirms the formation of the stacking faults and the coherent BZO/YBCO interface. Remarkably, the BZO 1D-APCs with a coherent interface with YBCO matrix exhibits wide angular pinning enhancement as demonstrated in the higher transported J_c (θ) and F_p (θ) at 65 K. For example, at B = 5 T and 9 T, the J_c data in the ML films are significantly higher than those of the SL films up to ~ 85°. Furthermore, $F_{p,max}$ data show pinning enhancements up to at least ~ 67°. Similarly, along B//c the $F_{p,max}$ enhancements are 1.7 and 4.4 for the 2% ML and the 6% ML respectively. The 6% ML also has 60% bigger B_{max} than the B_{max} of ~ 5.0 T of the 6% SL film. These results, together with the remarkable enhancement in pinning along B//c, demonstrates not only the critical importance of the BZO/YBCO interface in specific pinning efficiency of 1D-APCs, but also points to a viable approach to achieve it.

5. References

[1] Baca, F.J., et al., *Interactive Growth Effects of Rare-Earth Nanoparticles on Nanorod Formation in $YBa_2Cu_3O_x$ Thin Films.* Advanced Functional Materials, 2013. **23**(38): p. 4826-4831.

[2] Chen, S., et al., *Enhancement of isotropic pinning force in YBCO films with $BaZrO_3$ nanorods and Y_2O_3 nanoparticles.* IEEE Trans. Appl. Supercond, 2017. **27**(4): p. 4-8.

[3] MacManus-Driscoll, J., et al., *Strongly enhanced current densities in superconducting coated conductors of $YBa_2Cu_3O_{7-x}$+ $BaZrO_3$.* Nature materials, 2004. **3**(7): p. 439.

[4] Matsumoto, K. and P. Mele, *Artificial pinning center technology to enhance vortex pinning in YBCO coated conductors.* Superconductor Science and Technology, 2009. **23**(1): p. 014001.

[5] Wee, S.H., et al., *Engineering nanocolumnar defect configurations for optimized vortex pinning in high temperature superconducting nanocomposite wires.* Scientific Reports, 2013. **3**: p. 2310.

[6] Gautam, B., et al., *Microscopic adaptation of $BaHfO_3$ and Y_2O_3 artificial pinning centers for strong and isotropic pinning landscape in $YBa_2Cu_3O_{7-x}$ thin films.* Superconductor Science and Technology, 2018. **31**(2): p. 025008.

[7] Matsushita, T., *Flux pinning in superconducting 123 materials.* Superconductor Science and Technology, 2000. **13**(6): p. 730.

[8] Miura, S., et al., *Characteristics of high-performance $BaHfO_3$-doped $SmBa_2Cu_3O_y$ superconducting films fabricated with a seed layer and low-temperature growth.* Superconductor Science and Technology, 2015. **28**(6): p. 065013.
[9] Sebastian, M.A.P., et al., *Study of the flux pinning landscape of YBCO thin films with single and mixed phase additions $BaMO_3$+ Z: M= Hf, Sn, Zr and Z= Y_2O_3, Y211.* IEEE Transactions on Applied Superconductivity, 2017. **27**(4): p. 1-5.
[10] Tobita, H., et al., *Fabrication of $BaHfO_3$ doped $Gd_1Ba_2Cu_3O_{7-\delta}$ coated conductors with the high Ic of 85 A/cm-w under 3 T at liquid nitrogen temperature (77 K).* Superconductor Science and Technology, 2012. **25**(6): p. 062002.
[11] Mele, P., et al., *Ultra-high flux pinning properties of $BaMO_3$-doped $YBa_2Cu_3O_{7-x}$ thin films (M= Zr, Sn).* Superconductor Science and Technology, 2008. **21**(3): p. 032002.
[12] Varanasi, C., et al., *Thick $YBa_2Cu_3O_{7-x}$+ $BaSnO_3$ films with enhanced critical current density at high magnetic fields.* Applied Physics Letters, 2008. **93**(9): p. 092501.
[13] Feldmann, D., et al., *Improved flux pinning in $YBa_2Cu_3O_7$ with nanorods of the double perovskite Ba_2YNbO_6.* Superconductor Science and Technology, 2010. **23**(9): p. 095004.
[14] Opherden, L., et al., *Large pinning forces and matching effects in $YBa_2Cu_3O_{7-\delta}$ thin films with $Ba_2Y(Nb/Ta)O_6$ nano-precipitates.* Scientific reports, 2016. **6**: p. 21188.
[15] Foltyn, S., et al., *Materials science challenges for high-temperature superconducting wire.* Nature materials, 2007. **6**(9): p. 631.
[16] Gautam, B., et al., *Probing the effect of interface on vortex pinning efficiency of one-dimensional $BaZrO_3$ and $BaHfO_3$ artificial pinning centers in $YBa_2Cu_3O_{7-x}$ thin films.* Applied Physics Letters, 2018. **113**(21): p. 212602.
[17] Wu, J., et al., *Pinning Efficiency of One-Dimensional Artificial Pinning Centers in $YBa_2Cu_3O_{7-x}$ Thin Films*. Vol. 29. 2019. 1-5.
[18] Cantoni, C., et al., *Strain-driven oxygen deficiency in self-assembled, nanostructured, composite oxide films.* Acs Nano, 2011. **5**(6): p. 4783-4789.
[19] Blatter, G., et al., *Vortices in high-temperature superconductors.* Reviews of modern physics, 1994. **66**(4): p. 1125.
[20] Ogunjimi, V., et al. *The effect of APC/YBCO interface on the angular range of effective pinning by one-dimensional artificial pinning centers in $YBa_2Cu_3O_{7-x}$ nanocomposite films*. in *IOP Conference Series: Materials Science and Engineering*. 2020. IOP Publishing.
[21] Ogunjimi, V., et al., *The angular range of effective pinning by one-dimensional artificial pinning centers in $BaZrO_3/YBa_2Cu_3O_{7-x}$ nanocomposite films.* AIP Advances, 2019. **9**(8): p. 085110.
[22] Ogunjimi, V., et al., *Enhancing Magnetic Pinning by $BaZrO_3$ Nanorods Forming Coherent Interface by Strain-Directed Ca-doping in $YBa_2Cu_3O_{7-x}$ Nanocomposite Films.* Superconductor Science and Technology, 2021. 34 (10): p. 104002
[23] Baca, F.J., et al., *Control of $BaZrO_{(3)}$ nanorod alignment in $YBa_{(2)}Cu_{(3)}O_{(7-x)}$ thin films by microstructural modulation.* Applied Physics Letters, 2009. **94**(10): p. 3.
[24] Sebastian, M.A., et al., *Comparison Study of the Flux Pinning Enhancement of $YBa_2Cu_3O_{7-\delta}$ Thin Films With $BaHfO_3$ + Y_2O_3 Single- and Mixed-Phase Additions.* IEEE Transactions on Applied Superconductivity, 2019. **29**(5): p. 1-5.
[25] Wang, X., et al., *Eliminating thickness dependence of critical current density in $YBa_2Cu_3O_{7-x}$ films with aligned $BaZrO_3$ nanorods.* Journal of Applied Physics, 2010. **108**(11): p. 3911.
[26] Chen, S., et al., *Enhancement of Isotropic Pinning Force in YBCO Films With $BaZrO_3$ Nanorods and Y_2O_3 Nanoparticles.* IEEE Transactions on Applied Superconductivity, 2017. **27**(4): p. 1-5.
[27] Gautam, B., et al., *Microscopic Adaptation of $BaHfO_3$ and Y_2O_3 Artificial Pinning Centers for Strong and Isotropic Pinning Landscape in $YBa_2Cu_3O_{7-x}$ Thin Films.* Superconductor Science and Technology, 2017.
[28] Emergo, R.L.S., et al., *The effect of thickness and substrate tilt on the BZO splay and superconducting properties of $YBa_2Cu_3O_{7-\delta}$films.* Superconductor Science and Technology, 2010. **23**(11): p. 115010.
[29] Horide, T., M. Ishimaru, and K. Matsumoto, *Observation of inhomogeneous depinning in $YBa_2Cu_3O_7$ composite multilayers.* Superconductor Science and Technology, 2019. **32**(8): p. 085001.

[30] Horide, T., et al., *Hybrid artificial pinning centers of elongated-nanorods and segmented-nanorods in $Yba_2Cu_3O_7$ films.* Superconductor Science and Technology, 2016. **29**(10): p. 105010.
[31] Malmivirta, M., et al., *Enhanced flux pinning in YBCO multilayer films with BCO nanodots and segmented BZO nanorods.* Scientific reports, 2017. **7**(1): p. 1-8.
[32] Horide, T., et al., *Structural evolution induced by interfacial lattice mismatch in self-organized $YBa_2Cu_3O_{7-\delta}$ nanocomposite film.* ACS nano, 2017. **11**(2): p. 1780-1788.
[33] Shi, J.J. and J.Z. Wu, *Structural transition of secondary phase oxide nanorods in epitaxial $YBa_2Cu_3O_{7-\delta}$ films on vicinal substrates.* Philosophical Magazine, 2012. **92**(34): p. 4205-4214.
[34] Wu, J. and J. Shi, *Interactive modeling-synthesis-characterization approach towards controllable in situ self-assembly of artificial pinning centers in RE-123 films.* Superconductor Science and Technology, 2017. **30**(10): p. 103002.
[35] Wu, J.Z., et al., *The effect of lattice strain on the diameter of $BaZrO_3$ nanorods in epitaxial $YBa_2Cu_3O_{7-\delta}$ films.* Superconductor Science and Technology, 2014. **27**(4): p. 044010.
[36] Yoshida, Y., et al., *Approaches in controllable generation of artificial pinning center in $REBa_2Cu_3O_y$-coated conductor for high-flux pinning.* Superconductor Science and Technology, 2017. **30**(10): p. 104002.
[37] Khan, M.Z., et al., *Enhanced flux pinning isotropy by tuned nanosized defect network in superconducting $YBa_2Cu_3O_{6+x}$ films.* Scientific reports, 2019. **9**(1): p. 1-12.
[38] Samoilenkov, S., et al., *Anisotropic strain of $BaZrO_3$, $BaCeO_3$ and Y_2O_3 nanoinclusions in a $YBa_2Cu_3O_{7-x}$ epitaxial film matrix and its relation to the oxygen content of the superconductor.* Superconductor Science and Technology, 2011. **24**(5): p. 055003.
[39] Huhtinen, H., et al., *The effect of BZO doping concentration and thickness dependent properties of YBCO films grown by PLD on buffered NiW substrates.* Physica C: Superconductivity, 2012. **472**(1): p. 66-74.
[40] Huhtinen, H., et al., *Influence of $BaZrO_3$ dopant concentration on properties of $YBa_2Cu_3O_{6+x}$ films in magnetic fields up to 30 T.* Journal of Applied Physics, 2010. **107**(5): p. 053906.
[41] Jha, A.K., et al., *Tailoring the vortex pinning strength of YBCO thin films by systematic incorporation of hybrid artificial pinning centers.* Superconductor Science and Technology, 2015. **28**(11): p. 114004.
[42] Goyal, A., et al., *Irradiation-free, columnar defects comprised of self-assembled nanodots and nanorods resulting in strongly enhanced flux-pinning in $YBa_2Cu_3O_{7-\delta}$ films.* Superconductor Science and Technology, 2005. **18**(11): p. 1533.
[43] Gutierrez, J., et al., *Strong isotropic flux pinning in solution-derived $YBa_2Cu_3O_{7-x}$ nanocomposite superconductor films.* Nature materials, 2007. **6**(5): p. 367-373.
[44] Horide, T., et al., *Geometric and compositional factors on critical current density in $YBa_2Cu_3O_{7-\delta}$ films containing nanorods.* Superconductor Science and Technology, 2018. **31**(6): p. 065012.
[45] Wang, X., et al., *Eliminating thickness dependence of critical current density in $YBa_2Cu_3O_{7-x}$ films with aligned $BaZrO_3$ nanorods.* Journal of Applied Physics, 2010. **108**(11): p. 113911.

Acknowledgement
This research was supported in part by NSF contracts Nos: NSF-DMR-1508494 and 1909292 and NSF-ECCS-1809293, the AFRL Aerospace Systems Directorate, the Air Force Office of Scientific Research (AFOSR) LRIR #14RQO8COR and LRIR #18RQCOR100. D.Z. and H.W. acknowledge the support from the U.S. National Science Foundation for the high-resolution STEM effort at Purdue University (DMR-1565822 and DMR-2016453).